

pubs.acs.org/Macromolecules Article

A Multiscale Simulation Study of Influence of Morphology on Ion Transport in Block Copolymeric Ionic Liquids

Zidan Zhang, Jakub Krajniak, and Venkat Ganesan*

III Metrics & More



ACCESS I

Cite This: Macromolecules 2021, 54, 4997-5010



Article Recommendations

Homopolymer
MS1
MS2
MS3
MS4
Random copolymer

MS1
MS4
Random copolymer

MS1
MS4
Random copolymer

Fraction of interfacial anions

ABSTRACT: We present results of a multiscale simulation study involving coarse-graining and reverse-mapping steps probing at an atomistic resolution the influence of morphology on ion transport in block copolymer polymeric ionic liquids. We provide a detailed description of the multiscale simulation methodology and then describe the results in the context of four microphase-separated morphologies: two lamella systems, a cylinder, and a gyroid morphology. For the framework adopted in this study (in which the total number of ions was maintained fixed), morphology had little influence on the fraction of ions segregating to the interface and the coordination and hopping characteristics of such interfacially present ions. Such results manifested in anion mobilities being insensitive to the morphology once the dimensionality of the morphology was accounted for. Overall, our results are consistent with the hypothesis that the mobility of ions in such microphase-separated morphologies, after accounting for the dimensionality effects, can be roughly correlated to a linear superposition based on the fraction of bulk anions, which possess mobilities unperturbed from their values in the conducting homopolymers, and the interfacial anions, which exhibit much lower mobilities.

1. INTRODUCTION

In the past few decades, various types of polymer electrolytes have been extensively investigated in their potential for energy storage and electrochemical devices. 1-6 Despite promising advances in this regard, the generally lower conductivity of such materials have hindered their adoption in practical technological contexts. As a possible means to maintain sufficiently high conductivity simultaneously with mechanical strength, attention has turned toward designing block copolymeric electrolytes (BCP) composed of combinations of conductive and mechanically strong blocks. 7-16 It has been suggested that by appropriately choosing blocks to facilitate ion transport and mechanical strength and by tuning the morphology and domain sizes, such block copolymeric materials could overcome the trade-off between mechanical strength and conductivity underlying many polymer electrolytes. Motivated by such considerations, a number of studies have examined neutral block copolymers, charged block copolymers, and block copolymeric ionic liquids as potential candidates for a variety of energy applications. 16-20

Despite the vast number of studies on block copolymeric electrolytes, some outstanding questions still remain, especially on the role of morphology in influencing the conductivity in such systems. The most clarity in this regard has been achieved in the context of salt-doped neutral polymers, ^{13,16,21–26} in which a number of theoretical and experimental studies have shed light on the role of molecular weight, degree of segregation, and tortuosity of the morphology in influencing ion transport in such systems. In contrast, in systems such as polymeric ionic liquids and charged block copolymers, the physics underlying the influence of morphology on ion transport still remains to be clarified.

Supporting Information

Received: January 6, 2021 Revised: April 16, 2021 Published: May 27, 2021





The present study is concerned with the influence of morphology on ion transport in block copolymeric ionic liquids. Block copolymeric ionic liquids are emerging of interest as electrolyte materials combining the attractive properties and chemical stability of ionic liquids with the mechanical strength and morphological versatility afforded by the block copolymer architecture. 27-33 Based on such considerations, a number of experimental studies have examined the influence of morphology on the ion transport properties of polyIL-BCPs. 7-9,15,17,19,34-36 For instance, studies by Elabd, Winey, and co-workers observed that the ionic conductivities of microphase-separated polyIL BCPs were ~2 orders of magnitude higher than their random copolymer counterparts with the same composition of components.9 In a follow-up study, they found that the conductivity of the block copolymers was influenced by the degree of microphase separation.³⁴ In another study, Weber and co-workers demonstrated that the ionic conductivity depends on the morphology of microphase separation. More explicitly, they found that the conductivity of lamellae was ~5fold less than that of the homopolymer, and moreover, the conductivity of mixed phases of lamellar and cylinder morphologies was an order of magnitude lower than the lamellae.

While the above results appear superficially similar to those observed in salt-doped neutral block copolymers, 13,16,21-26 the mechanism of ion transport in polyILs is however distinct from salt-doped ILs. More explicitly, in salt-doped neutral polymers, 21,37-41 ion transport occurs from a combination of (i) intrachain ion motion along the polymer backbone, (ii) cooperative motion of ions coordinated with the polymer segments, and (iii) intersegmental hopping of ions from one chain to the other. As a result, the conductivity in neutral block copolymers is correlated to the fraction of ions segregated to the interface, a region also characterized by slower segmental dynamics and more pronounced ion aggregation. 21,23 In contrast, in polyIL systems, the motion of the counterion (with respect to the immobile ion tethered to the polymer) was found to involve a hopping process through a series of association-dissociation events involving four immobile ions from two polymer chains (for the specific chemistry investigated in our earlier work), 42-49 and as a result, the dynamics of the counterion is "partially" decoupled from polymer segmental dynamics.

Motivated by an objective to understand the mechanisms underlying in block copolymer polyILs, in our recent study, 46 we used a multiscale simulation framework to study, at an atomistic resolution, the physics underlying ion transport in a block copolymer polyIL in which the conductive domain consisted of 1-n-butyl,3-methylimidazolium hexafluorophosphate ([BmIm]+[PF₆]-) as the repeated units and the nonconductive domain contained methyl methacrylate (MMA) as repeated units. We found that the ion mobilities and conductivities decreased in the order homopolymer > lamellae > random copolymer. A detailed analysis of coordination and hopping mechanisms revealed that the interfacial area of the micorphase separated lamellae was characterized by frustrated anion-cation coordination behavior arising from the mixed presence of conducting and nonconducting units. Such modified coordination characteristics were shown to result in reduced ion hopping events and, consequently, lower mobile ion mobilities for the microphaseseparated morphologies.

The present work is motivated by two objectives: (i) to provide a more complete description of the multiscale approach and expand its implementation for other nonlamellar morphologies; (ii) to compare the results of ion mobilities for different morphologies to identify universal features, if any, underlying such properties. More specifically, on the basis of findings of our earlier work, 46 we hypothesize that the influence of morphology in ion transport in block copolymer polyIL systems is likely to exhibit features qualitatively similar to salt-doped neutral BCPs. Explicitly, we propose that the net influence of the morpholoy on ion mobilities will constitute two factors: (i) a dimensionality factor, which quantifies the tortuosity or the dimensional effects on transport, 24,25,50-52 and (ii) an interfacial factor which embodies the fraction of ions present in the interfacial region in such systems and the resulting impact on their transport.²⁶ By generating different morphologies and probing the ion mobilities in such systems, we propose to validate such an hypothesis in the context of polyILs. We note that this study is unique in its use of atomistically resolved simulations to study the above questions. Much of the other simulation studies discussed in the context of neutral block copolymers have been mostly based on coarsegrained simulations which may not accurately capture the details of ion coordination and transport characteristics.⁵³

The rest of this article is organized as follows: In section 2 we describe training procedure of the coarse-grained force field and the multiscale simulation framework. In section 3 we discuss the results of the density profiles of investigated morphologies, the properties of the interfacial region, and the ion mobilities. We conclude with a brief summary of our findings and conclusions in section 4.

2. MULTISCALE SIMULATION METHODOLOGY

To facilitate the study of ion transport mechanisms in microphase-separated morphologies, we developed a multiscale simulation approach that combines the advantages of coarse-grained (CG) simulations with the need for atomistic resolution to probe the mechanisms of ion transport. In a nutshell, our framework uses coarse-grained simulations to obtain the desired microphase-separated structures and then uses reverse mapping techniques to reintroduce the atomistic details. This concept was briefly introduced in our recent paper, and we present an expanded discussion in this section.

The multiscale simulation framework is accomplished by using a three-step procedure: (i) using an "ideal" CG bead–spring model to create initial morphologies, (ii) using a more specific CG representation where "real" CG potentials are used to equilibrate the system in the resulting morphologies, and (iii) using a reverse mapping method to convert the configuration of the "real" CG model to a fully atomistic representation. In the following sections we present a detailed overview and workflow relating to the three steps.

2.1. Step 1: Using an Ideal Coarse-Grained Model. In the first step, we generate templates of molecular configurations in expected morphologies using an "ideal" coarse-grained model that captures the broad physics of the block copolymer polyIL. Such a step is pursued since the "real" coarse-grained model (detailed in the next section) is still too complex to permit equilibration from random initial conditions into the appropriate microphase-separated morphologies. Hence, we use an ultracoarse-grained "ideal" model with a few adjustable parameters to achieve template configurations to serve as initial conditions for equilibrating the "real" coarse-

grained model. We note that different choices present for the coarse-grained models and simulation approaches can be used for constructing the template configurations as long as such models can result in microphase-separated morphologies and have the same coarse-grained topologies as the "real" coarse-grained model. In an earlier work of ours (in the context of salt-doped neutral polymers), 21 we used the single chain in mean-field theory (SCMF) 88-63 approach to accomplish this preliminary step.

In this study, we opted to use a bead–spring model based molecular dynamics simulations to implement the above step. More explicitly, for our system of polyILs, we use the harmonic bond potential to describe the bonded interactions; the nonbonded interactions among all the CG beads adopt Lennard-Jones (LJ) potentials. In this representation we do not consider angles, dihedral angles between beads, and the electrostatic interactions (this will be incorporated in the "real" CG model). For each of the systems, we vary the number of MMA and BvIm parts of the polymer chain to keep certain conductive domain volume fractions ($f(V_{\rm BvIm})$), as summarized in Table 1. (The LJ parameters for each morphology can be found in section S1 of the Supporting Information.)

Table 1. Details on the Number of Repeated Units per Polymer Chain for Different Morphologies (MS1–MS4) as Well as for Homopolymers (HO) and Random Copolymers (RA)^a

structure	НО	MS1	MS2	MS3	MS4	RA
$N_{ m MMA}$	0	20	60	60	20	20
$N_{ m BvIm}$	8	8	8	8	8	8
$f(V_{\mathrm{BvIm}})$	1.0	0.5	0.25	0.25	0.5	0.5

 $^{a}N_{\mathrm{MMA}}$ and N_{BvIm} are the number of units per polymer chain. $f(V_{\mathrm{BvIm}})$ is the conductive domain volume fraction. The $f(V_{\mathrm{BvIm}})$ for each morphology is calculated based on the volumes of repeated units at the atomistic resolution, as listed in Table 3.

We created four different morphologies based on the volume fraction $f(V_{\text{BvIm}})$. In addition, we also considered homopolymers (HO) and random copolymers (RA) for comparison of the ion transport properties. The initial configurations for all morphologies were constructed by packing polymer chains and counterions into the simulation box with the number density (in reduced unit) $\rho^*=0.85$. The total number of ion pairs is 1600, and the number of polymer chains in each of the system is 200. The charged systems were neutralized by adding 1600 counterions (PF₆⁻).

The lack of well-established phase diagrams for block copolymer polyILs presents challenges for the choice of coarsegrained parameters requisite for specified morphologies. Therefore, we tune both the bonded and nonbonded parameters of underlying block copolymer model to achieve lamella and cylindrical morphologies. For the determination each set of bonded and nonbonded parameters in LJ potential, we run a MD simulation to equilibrate the system. The MD simulation was performed by using leapfrog stochastic dynamics integrator with time step set to 2.0 τ (reduced unit). We run the simulation for 2.5×10^7 steps. Next, we investigated the final configuration by visual observation if the system represents one of the desired morphologies. To confirm it further, we calculated density profiles along different principal axes after converting the configuration to the "real" coarse-grained model (section S2, Supporting Information).

2.2. Step 2: Real Coarse-Grained Model. The morphologies obtained in step 1 are based on general Lennard-Jones interaction potentials and are not representative of the specific chemistry of the system chosen for our study. To provide a more precise description of the considered chemistry, a coarse-grained force field optimized for the polymer under consideration has to be employed. A number of strategies have been presented in the literature for developing such specific coarse-grained force fields: for instance, the forcematching method^{64,65} and thermodynamics-matching methods. 66,67 In our work, we chose the structure-matching method based on the iterative Boltzmann inversion (IBI) framework to obtain the "real" coarse-grained force fields. 68-71 The IBI method derives the effective pair potentials with the aim of reproducing the radial distribution functions g(r)s from the corresponding atomistic simulations (target properties). The iteration procedure takes the target properties (g(r)s) as the initial guess, and the effective pair potentials are updated until convergence between target g(r)s and g(r)s of the coarsegrained system.

Preparation of the Target Distributions. To perform the optimization of specific coarse-grained force field using the IBI method, the target distributions have to be prepared. We started from building the atomistic representation of two systems: the 1-n-butyl,3-methylimidazolium hexafluorophosphate ([BvIm]⁺[PF₆]⁻) and methyl methacrylate (MMA). Parameters for PBvIm and PF₆⁻ can be found in our previous studies, 42,43 and parameters for PMMA were derived by using the OPLS-AA force field parameters inside Gromacs's library⁷² (ver. 2018.4). The partial charges for PBvIm/PF₆⁻ and PMMA are reoptimized by using density functional theory at the B3LYP/6-311g**theory of level⁷³ with the Gaussian09 package.⁷⁶ The restrained electrostatic potential (RESP) was fitted through the Multiwfn package.⁷ These fitted charges have been further scaled down by a factor of 0.8 to have better dynamical properties in the simulation. 42,43

The topologies were generated by the MKTOP package⁷⁸ and revised manually. In both cases the degree of polymerization for both systems were set to 10. We packed randomly 200 polymer chains (and 2000 counterions in the case of PBvIm system) in the cubic box using packmol.⁷⁹ The leapfrog Verlet algorithm was utilized as the integrator. The time step was set to 1 fs. The nonbonded interactions were cut off at 1.1 nm. The particle-mesh method (PME)⁸⁰ was used to calculate electrostatic interactions. The temperature was set to 420 K and the pressure to 1 atm. We used a Nosé–Hoover thermostat⁸¹ with a coupling constant 0.5 ps and a Parrinello–Rahman barostat⁸² with a coupling constant set to 1.0 ps. The bonds containing the hydrogen atoms were restrained by using the LINCS method.⁸³ All simulations in this section were performed by using GROMACS 2018.4⁷²

A multistep equilibration procedure was used to prepare the equilibrated configuration for the production run: (1) energy minimization via steepest decent, (2) 0.5 ns NVT simulation at 600 K, (3) 0.5 ns NVT simulation at 420 K, and (4) 1 ns NPT simulation at 420 K and 1 bar. This procedure was looped until the final density did not change anymore. Such a preequilibrium procedure was inspired by the 21-step decompression method that has been proposed by Colina and coworkers, which could make the pre-equilibration much faster. S4,85 Finally, a 20 ns production was applied to collect the atomistic trajectory with the saving frequency at every 1 ps.

Optimization of Coarse-Grained Force Field. The "real" coarse-grained model is built based on the target distributions obtained from the above atomistic simulation. The target probability distributions of bonds, angles, and radial distributions of pair interaction are extracted from the trajectories and used as a target in the iterative training process. We divide the optimization process into two parts: First, we separately create the coarse-grained force fields for blocks PBvIm and PMMA. As a second step, we generate the parameters for interactions between these blocks using those optimized coarse-grained force fields.

The mapping scheme is designed for the purpose of dividing the PMMA and PBvIm repeated units at atomistic resolution into coarse-grained groups. Normally the design criterion of the mapping scheme is to make sure that the coarse-grained particles are easy to be identified by their functionalities, and ideally, the distributions (bond, angle, and radial distribution function) for interactions of the coarse-grained particles should be as simple as possible. With these considerations, the mapping scheme for PMMA and PBvIm repeated units is displayed in Figure 1.

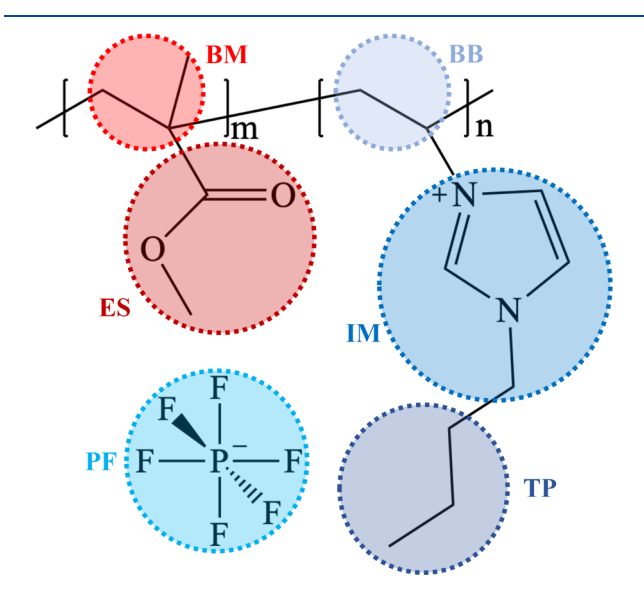


Figure 1. Coarse-grained (CG) mapping scheme for MMA block and BvIm block. MMA has been mapped into two CG beads BM and ES, BvIm⁺ has been mapped into three CG beads BB, IM, and TP, and the counterion PF₆⁻ has been mapped into one CG bead PF.

As depicted in the Figure 1, each MMA structural unit comprises of two coarse-grained particles: the backbone coarse-grained particle BM and the ester coarse-grained particle ES. In addition, each BvIm structural unit contains three coarse-grained particles: BB (the backbone group), IM (the methylimidazolium group), and TP (the propyl group) and with the additional free mobile counterion PF particle (PF_6^-) .

For the training method, we use the iterative Boltzmann inversion (IBI)⁶⁸ approach implemented in the VOTCA package.⁸⁶ The optimization procedure starts from the initial CG force field obtained from Boltzmann inversion given by the following equation

$$U(v) = -k_{\rm B}T \ln D(v) \tag{1}$$

where U is the potential function, $k_{\rm B}$ is the Boltzmann constant, and D is the probability distribution function of variable ν , which can be a bond length, bond angle, torsion angle, or radial distance. The initial potential, extracted in such way, cannot be directly used for the CG simulation. They should be adjusted to confront several changes from atomistic resolution to the coarse-grained resolution; that is, the coarse-grained particles are not charged, the solvent becomes implicit in the coarse-grained resolution, and the coarse-grained particles are fully spherical but the corresponding atomistic targets may not be. All these factors cause the derivation from the original force field parameters to their final values. The optimization of force field parameters is performed by iterative Boltzmann inversion (IBI), 68 which is explicitly described by eq 2. 87,88

$$U_{n+1}(v) = U_n(v) + \gamma k_B T \ln \frac{D_n(v)}{D_{\text{target}}(v)}$$
(2)

where $U_n(\nu)$ is the potential derived at step n, γ is the scale factor for tuning the increment for the potential of each step, $k_{\rm B}$ is the Boltzmann constant, T is temperature, $D_n(\nu)$ is the distribution function for the nth step, and $D_{\rm target}(\nu)$ is the target distribution function from atomistic simulation.

A short 1 ns NVT simulation was performed at every iteration step n. Langevin dynamics has been used for solving the equation of motion with a time step of 2 fs used during the simulation. A cutoff of 1.5 nm was set for nonbonded Lennard-Jones interactions. The temperature coupling method is the same as that in an atomistic system.

The optimization iterations were performed until the calculated distributions have good agreement with the target ones. The selected comparison between the target and the optimized distribution functions can be found in Figure 2 and the full comparison of all interactions can be found in the Supporting Information, section S3.

In the second step, we optimize the mixing parameters between blocks PBvIm and PMMA. The characteristic parameters (σ and ϵ) of each CG particle can be obtained by picking the first intersection to the x-axis and the first valley of the CG potential curve (the CG potential curves for CG particles are shown in section S2 of the Supporting Information), as listed in Table 2.

Then the CG force field between different blocks is fitted to the WCA potential: 89

$$U^{\mathrm{LJ/WCA}}(r_{ij}) = 4\epsilon_{ij} \left[\left(\frac{\sigma_{ij}}{r_{ij}} \right)^{12} - \left(\frac{\sigma_{ij}}{r_{ij}} \right)^{6} - \left(\frac{\sigma_{ij}}{r_{cij}} \right)^{12} + \left(\frac{\sigma_{ij}}{r_{cij}} \right)^{6} \right]$$
(3)

where σ_{ij} , ϵ_{ij} and r_{cij} are the effective diameter, interaction energy, and the potential cutoff for the interactions between species i and j. The parameters that involve different species $(\sigma_{ij} \text{ and } \epsilon_{ij})$ are generated by using the parameters in Table 2 by the Lorentz–Berthelot mixing rules; the r_{cij} for all the mixing parts is set to 1.12 nm. The resulting potential energy curves are shown in Figure 3. All the mixing potential energy curves are purely repulsive to maintain microphase-separated morphologies.

2.2.3. Converting from "Ideal" to "Real" Coarse-Grained Model. The "ideal" CG model presented in the first step of the multiscale simulation was a means to seed the desired morphologies. To accomplish the seeding process, we have

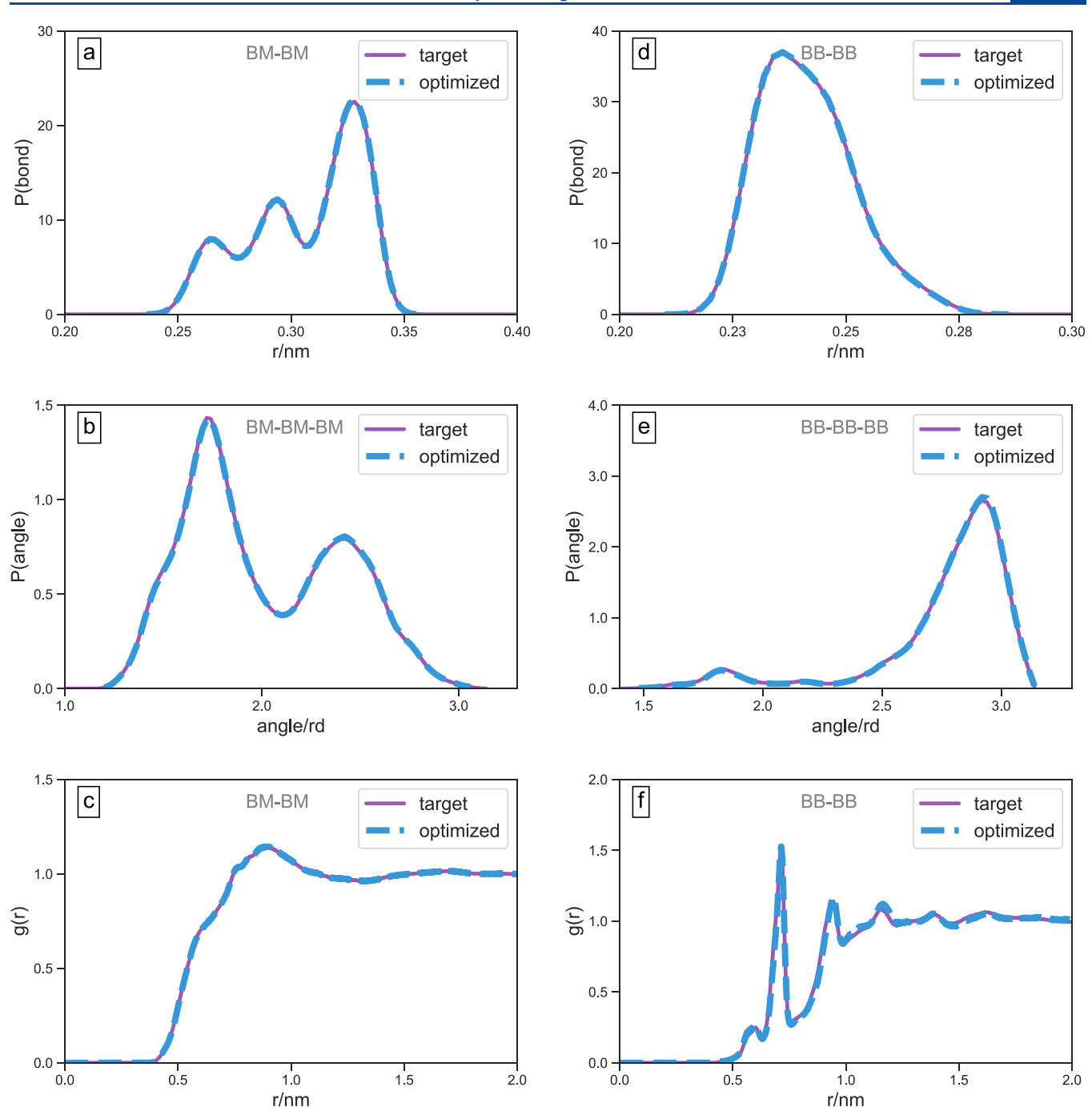


Figure 2. Selected bond, angle, and nonbonded distributions from atomistic simulation (target) and from IBI optimization (optimized) for PMMA (left panel) and for PBvIm (right panel). The full description of the comparison between the target and optimized distributions can be found in section S3 of the Supporting Information.

Table 2. Values for σ_{ii} and ϵ_{ii} Obtained through the Optimized Nonbonded Potentials

species	BM	ES	BB	IM	TP	PF
σ_{ii}/nm	0.56	0.49	0.65	0.53	0.48	0.64
$\epsilon_{ii}/\mathrm{kJ}\;\mathrm{mol}^{-1}$	-0.11	-1.28	-1.90	-0.99	-1.27	-1.05

to map the "ideal" model to a more realistic and more specific "real" model. Because the length units in the "ideal" and "real" CG model are different, we cannot simply replace the LJ potentials in the "ideal" model by the optimized CG force field because in both cases they are different. The "ideal"

representation is expressed in a typical nondimensional LJ units, whereas the "real" model uses nm as a length unit. Therefore, we have to rescale the ideal system to match the volume of the "real" model. The bridge was established by using the elemental volume of each repeat unit for the conversion of two coordinate systems, as shown in eq 4:

$$\mathbb{C}_{\text{CGMD}} = f \mathbb{C}_{\text{Ideal}}, \text{ where } f = \frac{n_{\text{PMMA}} V_{\text{PMMA}} + n_{\text{PBvIm}} V_{\text{PBvIm}}}{V_{\text{Ideal}}}$$
(4)

where n_{PMMA} and n_{PBvIm} are the number of molecules for PMMA and PBvIm, respectively, and V_{PMMA} and V_{PBvIm} are the

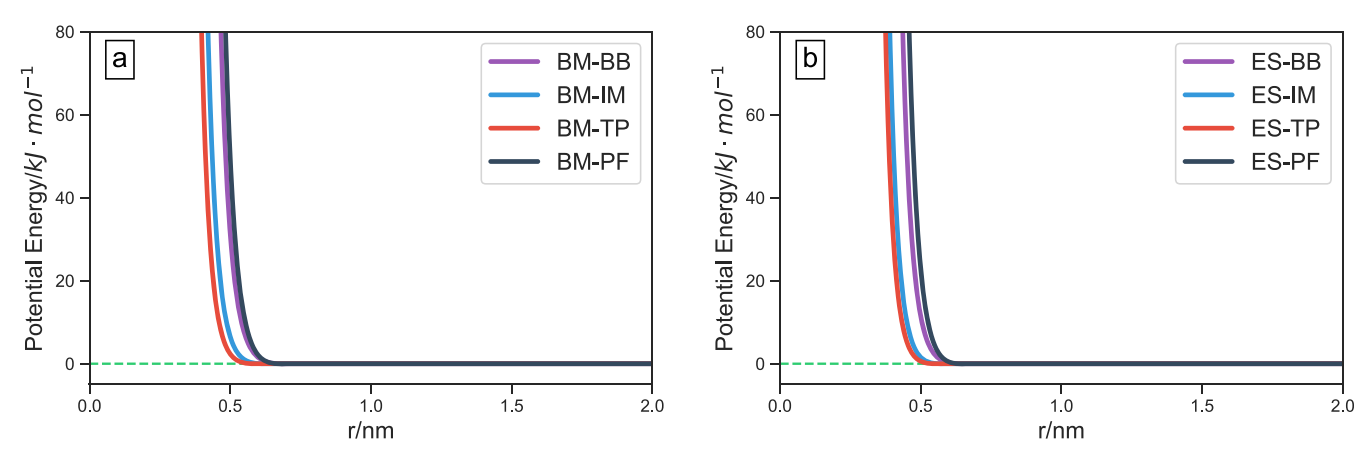


Figure 3. Generated pure repulsive potentials between particles from PMMA (BM and ES) and from PBvIm (BB, IM, TP, and PF) using eq 3 and parameters from Table 2.

molecular volumes, which can be obtained directly after the atomistic simulation implemented above, as listed in Table 3. $V_{\rm ideal}$ is the total volume of the "ideal" system. The positions of the particles as well as the size of the simulation box from the "ideal" system are rescaled by the factor f.

Table 3. Density and Elemental Volume Obtained from Atomistic Simulation of Individual PMMA and PBvIm Systems

species	$ ho/{ m g~cm^{-3}}$	$\nu/nm^3 \text{ mol}^{-1}$
PMMA	1.160	0.144
PBvIm	1.352	0.364

Next, the rescaled configuration for each of the morphologies was re-equilibrated by using the optimized "real" CG force field.

2.3. Step 3: Reverse Mapping to Atomistic Model. The third step of our multiscale simulation framework introduces chemical details via reverse mapping of the CG morphology. During the reverse mapping procedure, the coarse-grained representation is gradually transformed into the atomistic fined-grained resolution by using the adaptive reverse mapping method. ^{46,87,88,90,91} The details about the method can be found in the original papers. ^{90,91} For the sake of clarity, here we only recall the essential building blocks of the method.

To better understand the method, we first introduce the concept of an atomistic fragment, used in the rest of the paragraph. An atomistic fragment is a fine-grained representa-

tion of a coarse-grained bead. Each of the CG bead types has its own fragment. Technically, the fragment is a set of atom positions and a corresponding list of bonds, angles, dihedrals, and atom properties like mass and partial charges. The fragments are organized into a library, indexed by the coarse-grained bead type. Taking the conductive block PBvIm as example, as shown in Figure 4, the atomistic fragments for the BB, IM, and TP beads are prepared. The input coarse-grained configuration is nothing more than a list of CG bead positions for each of the CG bead types declared. This is accompanied by the list of bonds, angles, and dihedrals between the CG beads, which forms the topology.

The reverse mapping procedure is divided into two phases. In the preparation phase, the input coarse-grained configuration is enhanced with the position of atomistic particles. More explicitly, the list of CG beads is scanned, and for each of the CG beads an appropriate atomistic fragment from the library is selected and placed in the output trajectory. The position of the atoms in selected fragment is adjusted so that the fragment center-of-mass matches with the position of the CG bead. Along with the positions of atoms, the corresponding bonds, angles, and dihedrals are also copied to the output topology. By this, the "hybrid" configuration that contains both CG particles and AT particles has been generated, and the corresponding "hybrid" topology has also been generated.

The second phase of the procedure is the actual transition from the CG representation to the AT state. This is done by employing a hybrid adaptive resolution molecular dynamic

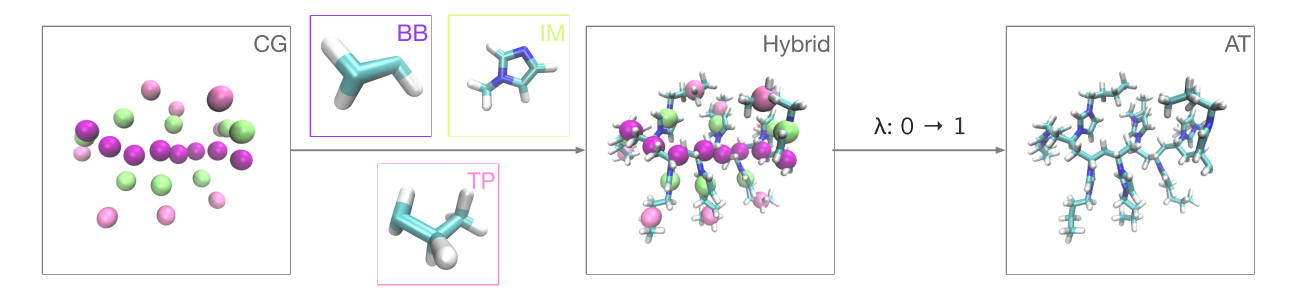


Figure 4. Illustration of the reverse mapping from coarse-grained resolution to atomistic resolution. By inserting the atomistic chemical fragments (BB, IM, and TP; cf. Figure 1) into the coarse-grained coordinates, a hybrid coordinate that contains both resolutions has been generated; then by use of eqs 5 and 6 in a hybrid adaptive resolution molecular dynamics simulation, the resolution of coarse-grained model has been gradually converted to an atomistic resolution (color scheme: purple = BB, green = IM, and pink = TP).

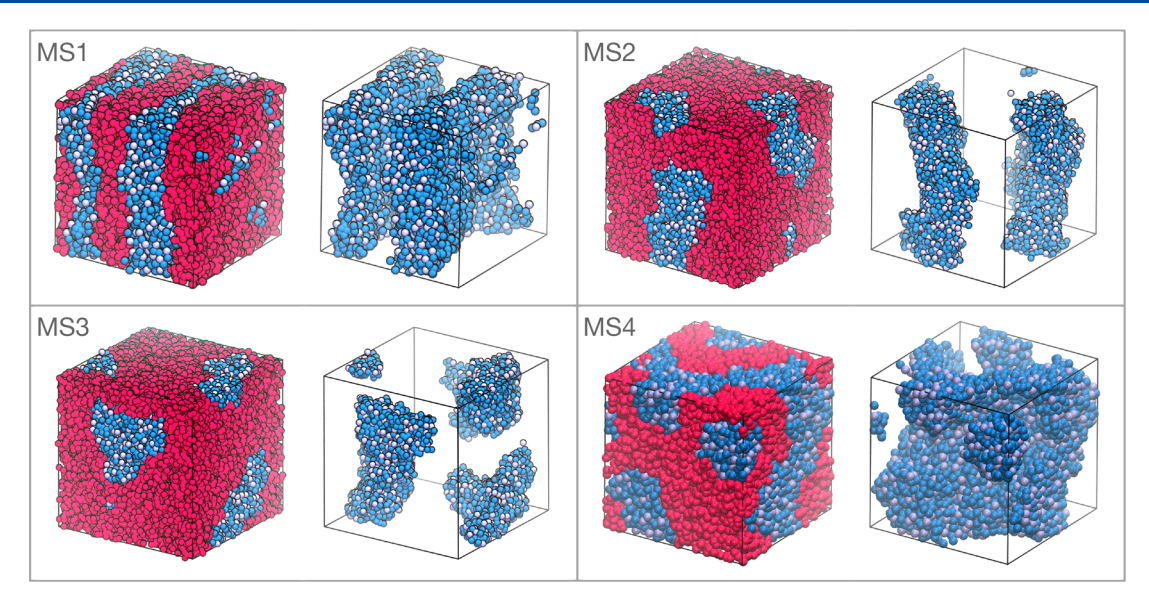


Figure 5. Illustration of the generated microphase-separated morphologies, the lamella-like MS1 and MS2, the cylindrical morphology MS3, and the gyroid-like MS4 (blue color indicates the conductive domain PBvIm, and the red color indicates the nonconductive domain PMMA). Other perspectives and periodically replicated images are presented in section S5 of the Supporting Information. (The configuration of MS1 was taken from our recently published paper, ⁴⁶ where MS1 has been referred to as LA.)

simulation, ⁹² governed by the in-house reverse mapping code ⁹³ (which is publicly available).

Each particle in the hybrid configuration has an associated parameter, λ , which controls the relative values of two parts of the interactions in the system: atomistic and coarse-grained. This could be better understood by considering the potential energy of the system, which is defined as

$$V(\mathbf{r}, t) = \underbrace{\lambda^{2}(t)[V_{\mathrm{I}}^{\mathrm{AT}}(\mathbf{r}) + V_{\mathrm{II}}^{\mathrm{AT}}(\mathbf{r})] + V(\mathbf{r})_{\mathrm{III}}^{\mathrm{AT}}}_{\text{atomistic}} + \underbrace{[1 - \lambda^{2}(t)][V_{\mathrm{I}}^{\mathrm{CG}}(\mathbf{C}) + V_{\mathrm{II}}^{\mathrm{CG}}(\mathbf{C})]}_{\text{coarse-grained}}$$
(5

where $V_{\rm I}$ are the nonbonded interactions, $V_{\rm II}$ are the bonded interactions, and $V_{\rm III}$ are the *scale-independent* bonded interactions. As we can see, by increasing the value of λ , we effectively remove the interactions between CG particles and at the same time we introduce the interactions between AT particles. The λ itself is updated during the simulation according to the equation

$$\lambda_{i+1} = \lambda_i + \alpha(t_{i+1} - t_0) \tag{6}$$

where α controls the rate at which the resolution is changed, t is the simulation time at step i+1, and t_0 is the simulation time when the reverse mapping procedure started. This effectively equilibrates the orientation and position of the fragments.

For the reverse mapping of the system of interest in this work we use following simulation parameters. The molecular dynamics was governed by the velocity-Verlet integrator accompanied by the Langevin thermostat. The time step was set to 2 fs. The cutoff for the long-range van der Waals interaction was 2.0 nm. The temperature was set to 420 K. The α parameter was set to 0.0002. We used the in-house 90,95 version of the ESPResSo++ molecular dynamics package. In the Supporting Information, we provide all necessary configuration files that allow reproducing the reverse mapping.

The morphologies resulting at 420 K at the atomistic resolution after reverse mapping match well to their "real"

coarse-grained counterparts (a validation for the reverse mapping procedure at 420 K between the "real" coarse-grained and atomistic model is shown in section S2 of the Supporting Information).

However, to probe the ion mobilities we re-equilibrated the system at 600 K and used the morphologies resulting therein. The latter equilibration lasts for 20 ns, and by examining the density profiles, we concluded that the system was equilibrated in the desired temperature (see section S4, Supporting Information). This was followed by 200 ns of a production run which was later analyzed, and the results are reported in the next sections. The production run was performed by using the GROMACS 2018.4⁷² package.

2.4. Quantification Measures. *Radial Distribution Functions.* The structural characteristics of different particle species (cf. the mapping scheme in Figure 1) were quantified by calculating the ion pair radial distribution function utilizing

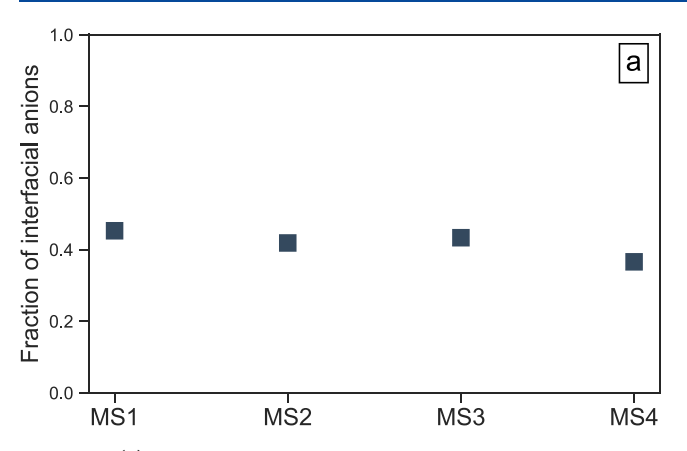
$$g_{ij}(r) = \frac{V}{4\pi r^2 N_i N_j} \langle \sum_{i}^{N_i} \sum_{j}^{N_j} \delta(r - r_{ij}) \rangle$$
(7)

where N_i and N_j are the number of particle species i and j. V is the volume of simulation box, and δ is the Dirac delta function. r is the position between the center-of-mass of particles i and j. In addition, the cutoffs for investigating the anion—polycation association characteristics in different morphologies were determined by the position r where g(r)=1.0 after the first peak.

Diffusion Tensor. The transport properties of the anion PF_6^- were probed by the diffusivity tensor that was derived from the corresponding mean-square displacement (MSD) and the Einstein relation:

$$\mathbf{D}_{PF_6^-} = \lim_{t \to +\infty} \frac{1}{6t} \{ (\vec{R}_{PF_6^-}(t) - \vec{R}_{PF_6^-}(0)) (\vec{R}_{PF_6^-}(t) - \vec{R}_{PF_6^-}(0)) \}$$
(8)

where \vec{R} is the position vector of the center-of-mass of anion PF_6^- . The diffusivity of the polycation $BvIm^+$ was not considered because in our recent study we found that even



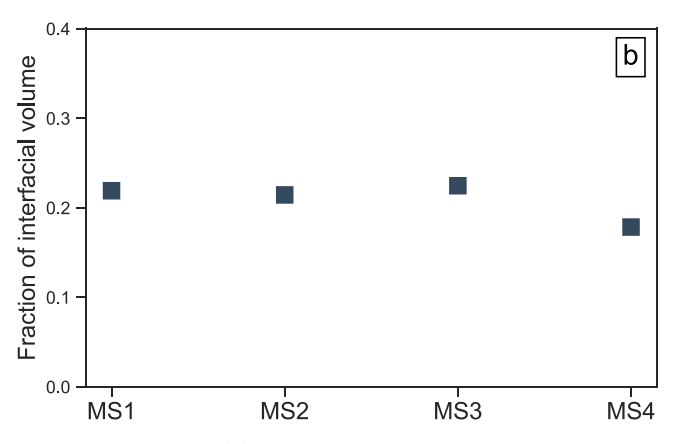


Figure 6. (a) Fraction of anions that are located near the interface for different morphologies. (b) Fraction of interfacial volume for different morphologies.

with relatively long time simulation times extending 400 ns, polycation diffusivities are not easy to obtain for longer polymer chains.⁹⁷

Considering different morphologies have different shapes of conductive domain and that such conductive domains may not be aligned along the coordinate axis, the anion PF₆⁻ diffusion was quantified by the eigenvalues of diffusion tensor **D**, where

$$\mathbf{D} = \mathbf{v} \cdot \mathbf{\Lambda} \cdot \mathbf{v}^{\mathrm{T}} \tag{9}$$

where **v** is the eigenvector and Λ ($\Lambda = [\lambda_1, \lambda_2, \lambda_3]$) are the eigenvalues of the of diffusion tensor **D**.

Generally speaking, in homogeneous morphologies, such as resulting in homopolymers and random copolymers, the diagonal terms in the diffusion tensor **D** eigenvalues are equal and the off-diagonal terms are zero. For anisotropic morphologies such as lamellae and cylinder, the off-diagonal terms are nonzero, the eigenvalues are equal to the principal diffusivity values, and the eigenvectors quantify the orientation of the morphologies.

3. RESULTS AND DISCUSSION

3.1. Morphologies Generated. As discussed in section 2.1, we seeded the real CG simulations with lamella and cylindrical morphological morphologies arising in our ideal CG simulations. However, such morphologies are to be viewed as "initial conditions" and may not necessarily persist upon equilibration with the real CG model. In Figure 5, we present the final morphologies resulting from the equilibration of the real coarse-grained model. On the basis of visual observations (other perspectives and periodically replicated images are presented in section S5 of the Supporting Information), it is evident that MS1 represents a lamella morphology and MS3 represents a cylindrical morphology. The morphology MS2 appears to possess elements of both lamella and cylindrical characteristics and is identified as a broken lamella morphology (see Figure S10). While not conclusive, MS4 presents a connected morphology similar to the gyroid phase. While a more conclusive confirmation of the morphologies may be achieved by computing the structure factors, the small size of our simulation cell precludes such an approach. However, in section 3.4, we present results for the diffusivity tensor which confirm the conclusions derived from visual observations.

3.2. Interfacial Anions and Interfacial Volume. In our recent study, 46 we considered the ion transport mechanisms in lamellar morphologies of polyIL block copolymers to

demonstrate that the influence of microphase separation primarily arises due to the modified coordination and hopping features that manifest in the interfacial zones of lamella. As a first step toward identifying universal rules governing the influence of different morphologies on the ion transport properties, we identify the interfacial regions and the corresponding number of anions in such regions for the structures MS1, MS2, MS3, and MS4.

In our recent study,⁴⁶ we used a definition of the interfacial area that relied on the use of a fit of the density profiles. However, such a procedure is harder to implement for the lamellar morphology (MS2) where the conductive domain was not aligned to the coordinate plane or the nonlamellar morphologies MS3 and MS4. Instead, in this work we use an alternative way for defining the interfacial region and the interfacial anions. In this approach, whenever a given anion is close to an ester unit (ES) within the cutoff range (0.63 nm), it is counted as an interfacial anion (the definition of the first coordinate shell is shown in section S6 of the Supporting Information). If no ES unit can be found in the cutoff range of the given anion, the anion will be defined as a bulk anion.

In addition, the fraction occupied by interfacial volume was also calculated. The fraction of the interfacial volume is defined as

$$f_{\rm iv} = \frac{V_{\rm interfacial \, volume}}{V_{\rm BvIm}} \tag{10} \label{eq:five_potential}$$

where $V_{\rm interfacial\ volume}$ is the product of the number density maps (in the grid form) for a nonconductive domain (PMMA) and a conductive domain (PBvIm) and $V_{\rm BvIm}$ is the volume of the conductive domain (cf. section S7 of the Supporting Information).

In Figure 6a, we present the results for the fraction of anions located in the interfacial region of different morphologies. Surprisingly, we find that the number (and fraction) of interfacial anions is insensitive to the actual morphology and is within a narrow range of 0.37 (MS4)–0.45 (MS1). Similarly, we observe that the fraction of volume occupied by the interfacial region (Figure 6b) is also insensitive to the morphology and is in the range 0.17 (MS4)–0.22 (MS1). We speculate that such insensitiveness arises from the fact that our simulation framework maintains the same number of total ion pairs across the different morphologies.

Together, the results presented in this section demonstrate that both the number of anions that are located near the

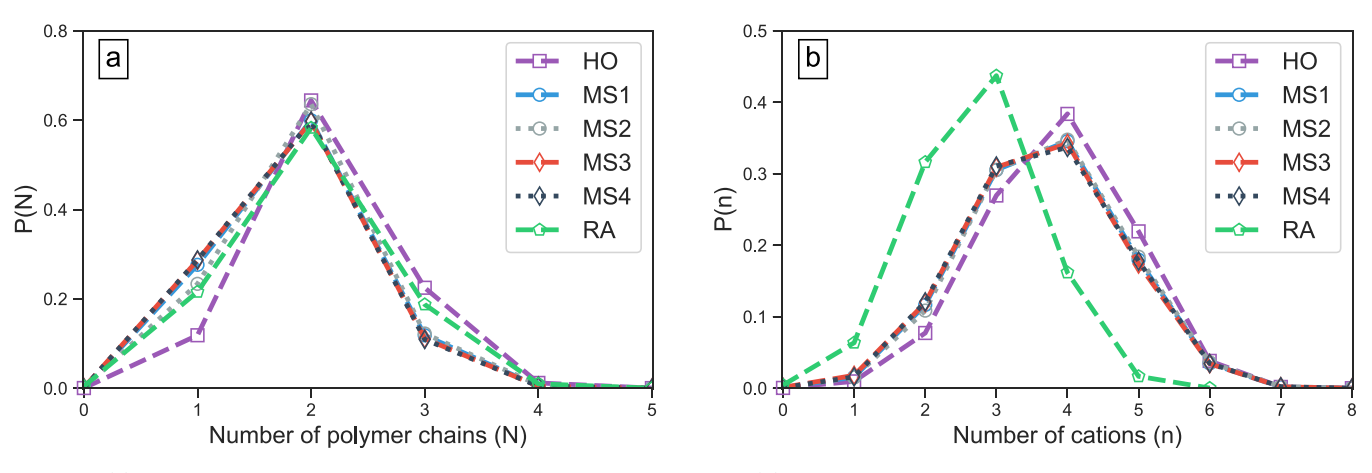


Figure 7. (a) Probability that a given anion is associated with N polymer chains. (b) Probability that a given anion is associated n cations. The data for HO, MS1, and RA are borrowed from our recent study.

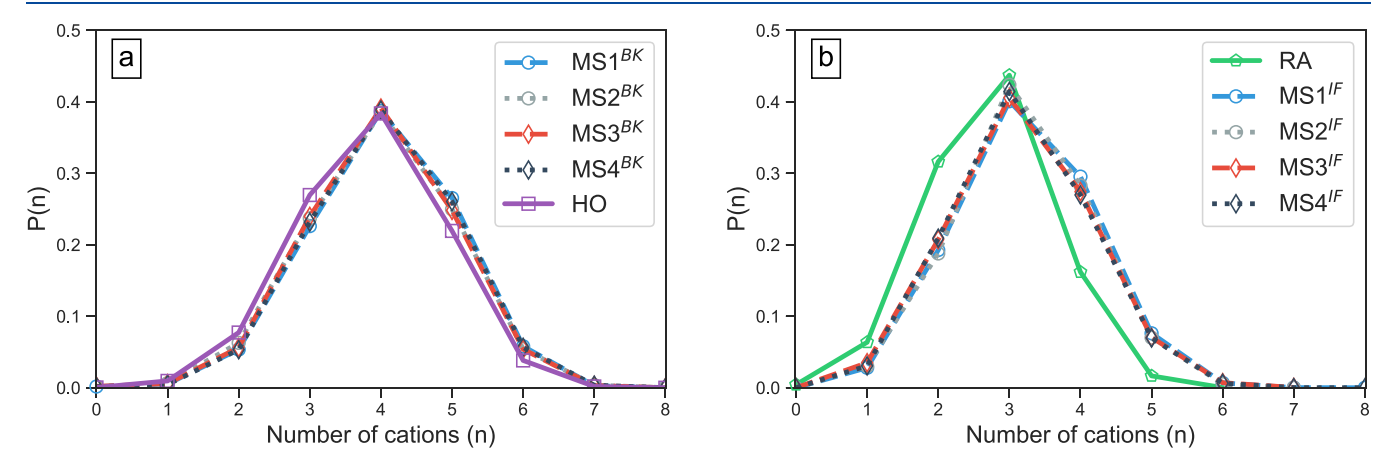


Figure 8. (a) Probability that an given anion in the bulk region (BK) is associated with n cations. (b) Probability that an given anion in the interfacial region (IF) is associated with n cations. The data for HO and RA are borrowed from our recent study; ⁴⁶ however, the data for MS1 in the bulk region and interfacial region are recalculated based on the new definition of interfacial anions which has been mentioned in section 3.2.

interface and the fractional volume occupied by the interface are comparable for the different morphologies. In the next section, we present results probing whether the ion transport mechanism coordination characteristics themselves are influenced by the morphology.

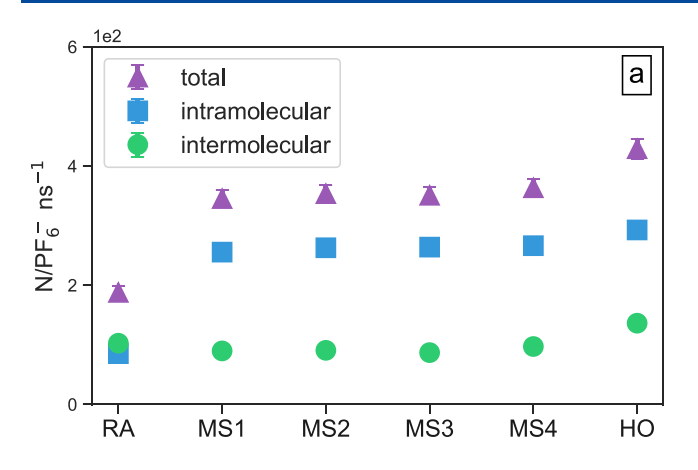
3.3. Influence of Morphology on Ion Transport Mechanisms. In our earlier studies 42-49 on polyILs, we had used the anion-cation coordination characteristics as an important feature to probe ion transport mechanisms. More explicitly, the anion-cation interactions were quantified by the use of two probability distributions: (i) P(N), which embodies the probability that a given anion is associated with N polymer chains; (ii) P(n), which embodies the probability that a given anion is associated with n cations. For homopolymer polyILs, our past studies demonstrated that P(N) and P(n) exhibit maxima at N = 2 and n = 4, respectively. 42,43 On the basis of such results, it was concluded that in polyIL systems the motion of counterion involves a hopping process through a series of association-dissociation events involving four polycations from two polymer chains. In our earlier study which examined the lamella morphology of block copolymer polyILs, 46 the analysis of ion pair association revealed that the P(n) for interfacial area was characterized frustrated coordination behavior, which resembles the association characteristics in random copolymer RA. Such modified ion pair association

characteristics were shown to lead to reduced ion hopping events and lower mobile ion mobilities.

In an effort to shed light on the influence of morphology on the ion transport mechanisms, in Figure 7 we display the probabilities of P(N) and p(n) for the different morphologies that have been considered in this study. The results presented in Figure 7a indicate that in all investigated morphologies the anion prefers to associate with two polymer chains. Such a result is similar to the results noted in our previous studies for homopolymer systems 42,43,46 and demonstrates that morphology does not influence the anion coordination distribution with respect to the polymer chains.

In Figure 7b, we display the anion—cation association probabilities p(n) among different morphologies. For the microphase-separated morphologies, a broad distribution with comparable peak probabilities between n=3 and n=4 can be observed. More pertinently, it can be seen that the results of p(n) are independent of the morphology under consideration.

To further analyze the above results for p(n), we separately consider the anions located in the interface and the bulk regions and catalog the respective probability distributions (Figure 8). We can see that the probability distributions of the bulk region anions reproduce the features that characteristic of the homopolymer (HO) and display a peak at n = 4. In contrast, the anions located at the interface display a peak at n = 3. Interestingly, even the probability distributions for the



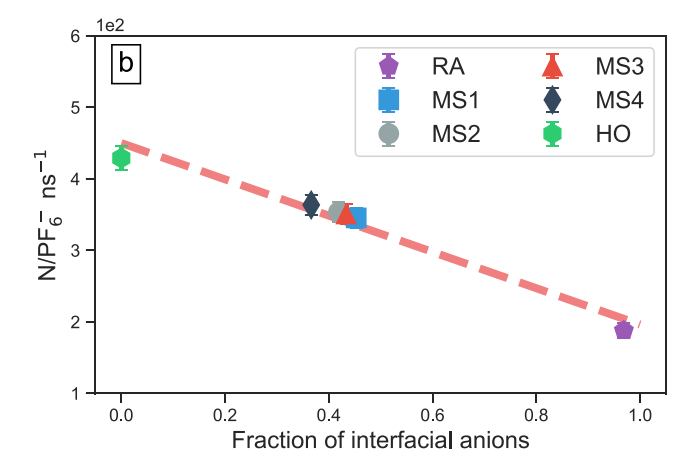


Figure 9. (a) Average hopping events of a given PF_6^- in unit time period. (b) Total hopping events as a function of the fraction of anions that are located near the interface. The data for HO, MS1, and RA are borrowed from our recent study.

Table 4. Eigenvalues of Diffusion Coefficients Calculated from the Mean-Square Displacement Tensor for Three Principal Axes T

eigenvalues	НО	MS1	MS2	MS3	MS4	RA
$T_1/\text{cm}^2 \text{ s}^{-1}$	5.914×10^{-8}	2.216×10^{-8}	2.306×10^{-8}	1.965×10^{-8}	2.329×10^{-8}	2.890×10^{-9}
$T_2/\text{cm}^2 \text{ s}^{-1}$	5.733×10^{-8}	1.981×10^{-8}	2.002×10^{-8}	1.531×10^{-8}	2.146×10^{-8}	2.813×10^{-9}
$T_3/{\rm cm}^2~{\rm s}^{-1}$	5.397×10^{-8}	1.046×10^{-8}	1.008×10^{-8}	1.107×10^{-8}	2.011×10^{-8}	2.641×10^{-9}
dimensional	3D	2D	2D	1D	3D	3D

anions located in the interface are seen to not display any dependence on the morphology. On the basis of these results, it can be deduced that the results of Figure 7b arise from a combination of the coordination characteristics of the bulk and interfacial anions.

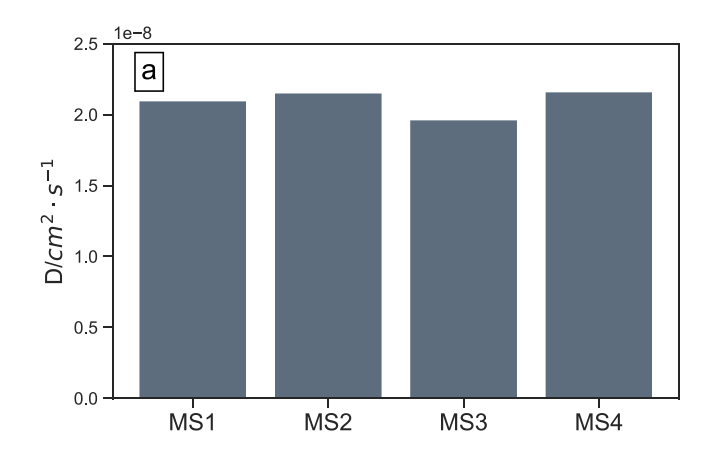
Together, the above results demonstrate that the coordination statistics of the anions in the microphase-separated morphologies, while different from that of the homopolymer, are not sensitive to the morphology themselves. As a result, we expect that the ion transport mechanisms (hopping characteristics) also to be insensitive to the morphology. Such expectations are confirmed in the results displayed in Figure 9. Explicitly, in Figure 9a it can be seen that the intramolecular and intermolecular hopping rates converge at the same level for microphase-separated morphologies. In addition, in Figure 9b we display the total number of hopping events as a function of the fraction of interfacial anions. (The HO corresponds to a case of 0.0 due to a lack of interfaces, and RA corresponds to a value of 0.97 based on our definition of identifying interfacial anions.) Therein, it can be observed that the number of hopping events in microphase-separated morphologies can be rationalized as a combination of the interfacial characteristics that resemble a random copolymer (RA) and the bulk characteristics that resemble a homopolymer (HO).⁴⁶

At a physical level, the insensitiveness of ion coordination and hopping characteristics to morphology can be rationalized by noting that the coordination and transport of the anions occur on length scales that are much smaller than the interfacial widths. Hence, differences in chain statistics arising from the different morphologies are less likely to be of strong influence on the ion coordination behavior. Instead, the coordination statistics in microphase-separated systems are likely to primarily reflect the mixed environment involving the presence of both 1-n-butyl,3-methylimidazolium hexafluorophosphate (BvIm) and methyl methacrylate (MMA). Hence, it is not surprising that the coordination and hopping character-

istics in the interfacial regions of the block copolymer polyILs exhibit strong similarities to the results for RA (Figures 8 and 9b).

3.4. Anion Mobilities. We are now positioned to examine the central hypothesis presented in the beginning of this study. To recall, we had proposed that the influence of morphology on anion mobilities is expected to involve a combination of a dimensionality factor arising from the confinement and tortuosity of the morphology and an interfacial factor arising from the modified coordination/hopping characteristics in the interfacial regions. The results presented in the preceding two sections demonstrated that for the morphologies and framework considered in this study both the number of anions and the mechanisms of ion transport in the interfacial region exhibit only a very weak dependence on the actual morphology itself. In addition, the results from hopping analysis (Figure 9b) suggested that the total hopping events exhibit an approximately linear correlation to the fraction of interfacial anions. Hence, we expect that once the morphological factor is accounted for, the anion mobilities in the different morphologies should be nearly identical for the different systems considered in our study and correlated to the fraction of interfacial anions.

Considering the three-dimensional nature of the different microphase-separated morphologies, we calculated the principal components of the diffusion tensor obtained as the eigenvalues of $\bf D$ using eq 9. (The overall mean-square displacement of ${\rm PF_6}^-$ in investigated systems can be found in section S8 of the Supporting Information, and the detailed eigenvalues and corresponding eigenvectors are shown in section S9 of the Supporting Information.) In a truly homogeneous system, the diagonal elements are expected to be equal, and the off-diagonal elements should be zero. Similar to the homogeneous system, transport in gyroid structure would have three comparable eigenvalues. In contrast, in lamella systems, in which the transport primarily occurs in two



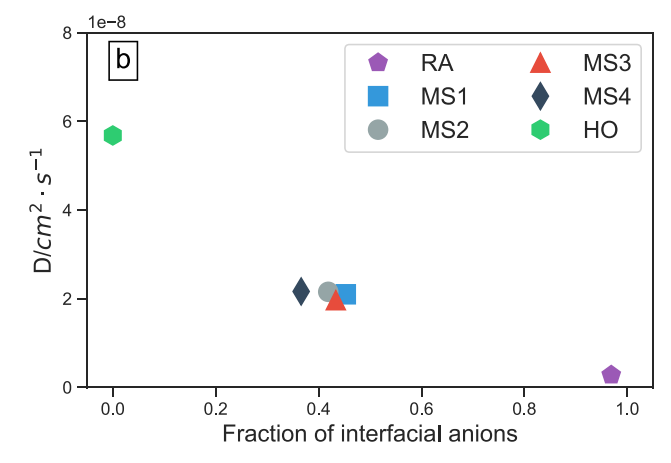


Figure 10. (a) Histogram of the eigenvalues of 1-dimensional diffusivity for microphase-separated morphologies. (b) Eigenvalues of one-dimensional diffusivity as a function of fraction of anions that are located near the interface.

dimensions, two of the eigenvalues are expected to be equal and much larger than the third one. Finally, in cylindrical morphologies, in which transport occurs predominantly in one dimension, a single eigenvalue is expected to be dominant and the remaining two are much smaller.

In Table 4, we list the self-diffusion coefficients for the different morphologies along three principal axes. On the basis of the considerations discussed in the preceding paragraph, we confirm that HO and RA systems are homogeneous systems since all three eigenvalues are comparable to each other. Consistent with the results of our earlier study, 46 we observe that the ion mobilities in RA are much lower than those in HO systems.

In the MS1 case, two of the eigenvalues are observed to be notably larger than the third one, indicating that ion transport in such systems is two-dimensional in nature. In the MS2 case, we observe two of the eigenvalues are larger than the third, suggestive of a lamella morphology (we recall that the visual observations suggested a mixture of lamella and cylindrical phases). For the MS3 case, there is a single dominant eigenvalue, indicating that ion transport in such systems is predominantly one-dimensional. As expected, the gyroid MS4 case seems to resemble a homogeneous system as well, but with the overall diffusion coefficient smaller than that in HO.

Based on the identification of the dimensional nature of transport in the constructed morphologies, a comparison can be effected of the true influence of morphology on the overall ion transport. The one-dimensional diffusion coefficient (calculated as the average of major eigenvalues) is shown in Figure 10a as a function of the morphology. From the result, we can see that the one-dimensional diffusion coefficients align at the same level (around $2.1 \times 10^{-8} \text{ cm}^2 \text{ s}^{-1}$) and are almost independent of the morphology underlying the block copolymer. In addition, the diffusivity of the different morphologies (cf. Figure 10b) is seen to fall in a roughly linear correlation to the fraction of anions located in the interfacial region.

The above results serve to partially validate the hypothesis discussed in the beginning of this section. Explicitly, the results of Figures 10a and 10b demonstrate that once the morphological factor is accounted, the overall diffusivity of the anions can be understood to arise as a combination of two factors: the "bulk" anions, which display coordination characteristics identical with that of homopolymer systems,

and hence possess mobilities which are unperturbed from their HO values, and the "interfacial" anions, which display modified coordination characteristics arising due to the mixed chemical nature of the interface. Such interfacial characteristics resemble that of RA (albeit, not identical with RA) and result in much lower mobilities for the anions.

Admittedly, a stronger support for our hypothesis could have benefitted from parametric conditions in which the number of anions in the interfacial region does show a stronger dependence on the morphology. In a future study, we hope to undertake other parametric conditions where the number of interfacial anions could be varied over different morphologies to study whether the linear correlation noted in Figure 10b holds more generally.

4. CONCLUSIONS

In this article, we presented results following up on our earlier study⁴⁶ focusing on an extended investigation of the influence of morphology on ion transport in block copolymer polyILs. We presented a more detailed description of the multiscale simulation methodology and then described the results in the context of four microphase-separated morphologies. For the framework adopted in this study (in which the total number of ions was maintained fixed), morphology had little influence on both the fraction of ions segregating to the interface and the coordination characteristics of such interfacially present ions. Such results manifested in anion mobilities being insensitive to the morphology once the dimensionality of the morphology was accounted. Overall, our results were consistent with the hypothesis that the mobility of ions in such microphaseseparated morphologies, after accounting for the dimensionality effects, can be roughly correlated to a linear superposition based on the fraction of bulk anions that possess mobilities which are unperturbed from their HO values and the interfacial anions which exhibit much lower mobilities. In future studies, we hope to undertake a broader exploration of the morphological phase diagram to explore parametric conditions in which both the interfacial segregation and the mechanisms of ion transport in the interface are influenced by the morphology.

ASSOCIATED CONTENT

Supporting Information

The Supporting Information is available free of charge at https://pubs.acs.org/doi/10.1021/acs.macromol.1c00025.

Section S1: the coarse-grained parameters for "ideal" model; section S2: the density profiles for microphase-separated structures; section S3: the optimized coarse-grained force field using IBI; section S4: the total density profiles of investigated systems at 600 K; section S5: configurations for microphase-separated morphologies; section S6: the definition of the first coordinate shell; section S7: volume of conductive domain and interfacial volume; section S8: the overall mean-square displacement of PF_6^- in investigated systems; section S9: the dimensional diffusivity and the corresponding eigenvector (PDF)

AUTHOR INFORMATION

Corresponding Author

Venkat Ganesan — McKetta Department of Chemical Engineering, University of Texas at Austin, Austin, Texas 78712, United States; orcid.org/0000-0003-3899-5843; Email: venkat@che.utexas.edu

Authors

Zidan Zhang — McKetta Department of Chemical Engineering, University of Texas at Austin, Austin, Texas 78712, United States; orcid.org/0000-0002-6909-8742

Jakub Krajniak – Independent researcher, 61-631 Poznan, Poland; o orcid.org/0000-0001-9372-6975

Complete contact information is available at: https://pubs.acs.org/10.1021/acs.macromol.1c00025

Notes

The authors declare no competing financial interest.

■ ACKNOWLEDGMENTS

The authors' work on the topic of ion transport in polymer electrolytes has been generously supported by grants from the Robert A. Welch Foundation (Grant F1599) and the National Science Foundation (CBET-1706968 and DMR-1721512). The development of the multiscale simulation methodology was supported as part of the Center for Materials for Water and Energy Systems, an Energy Frontier Research Center funded by the U.S. Department of Energy, Office of Science, Basic Energy Sciences, under Award #DE-SC0019272. The authors acknowledge the Texas Advanced Computing Center (TACC) for the generous allocation of computing resources.

REFERENCES

- (1) Fadel, E. R.; Faglioni, F.; Samsonidze, G.; Molinari, N.; Merinov, B. V.; Goddard, W. A., III; Grossman, J. C.; Mailoa, J. P.; Kozinsky, B. Role of solvent-anion charge transfer in oxidative degradation of battery electrolytes. *Nat. Commun.* **2019**, *10*, 3360.
- (2) Ganesan, V. Ion transport in polymeric ionic liquids: recent developments and open questions. *Molecular Systems Design & Engineering* **2019**, *4*, 280–293.
- (3) Park, M. J. Confinement-entitled morphology and ion transport in ion-containing polymers. *Molecular Systems Design & Engineering* **2019**, *4*, 239–251.
- (4) Mecerreyes, D.; Porcarelli, L.; Casado, N. Innovative Polymers for Next-Generation Batteries. *Macromol. Chem. Phys.* **2020**, 221, 1900490.

- (5) Wang, X.; Kerr, R.; Chen, F.; Goujon, N.; Pringle, J. M.; Mecerreyes, D.; Forsyth, M.; Howlett, P. C. Toward High-Energy-Density Lithium Metal Batteries: Opportunities and Challenges for Solid Organic Electrolytes. *Adv. Mater.* **2020**, *32*, 1905219.
- (6) Kang, S.; Park, M. J. 100th Anniversary of Macromolecular Science Viewpoint: Block Copolymers with Tethered Acid Groups: Challenges and Opportunities. ACS Macro Lett. 2020, 9, 1527–1541.
- (7) Weber, R. L.; Ye, Y.; Schmitt, A. L.; Banik, S. M.; Elabd, Y. A.; Mahanthappa, M. K. Effect of Nanoscale Morphology on the Conductivity of Polymerized Ionic Liquid Block Copolymers. *Macromolecules* **2011**, *44*, 5727–5735.
- (8) Elabd, Y. A.; Hickner, M. A. Block Copolymers for Fuel Cells. *Macromolecules* **2011**, *44*, 1–11.
- (9) Ye, Y.; Choi, J.-H.; Winey, K. I.; Elabd, Y. A. Polymerized Ionic Liquid Block and Random Copolymers: Effect of Weak Microphase Separation on Ion Transport. *Macromolecules* **2012**, *45*, 7027–7035.
- (10) Ozcam, A. E.; Petzetakis, N.; Silverman, S.; Jha, A. K.; Balsara, N. P. Relationship between Segregation Strength and Permeability of Ethanol/Water Mixtures through Block Copolymer Membranes. *Macromolecules* **2013**, *46*, 9652–9658.
- (11) Kim, O.; Jo, G.; Park, Y. J.; Kim, S.; Park, M. J. Ion Transport Properties of Self-Assembled Polymer Electrolytes: The Role of Confinement and Interface. *J. Phys. Chem. Lett.* **2013**, *4*, 2111–2117.
- (12) Bouchet, R.; Maria, S.; Meziane, R.; Aboulaich, A.; Lienafa, L.; Bonnet, J.-P.; Phan, T. N. T.; Bertin, D.; Gigmes, D.; Devaux, D.; Denoyel, R.; Armand, M. Single-ion BAB triblock copolymers as highly efficient electrolytes for lithium-metal batteries. *Nat. Mater.* **2013**, *12*, 452.
- (13) Inceoglu, S.; Rojas, A. A.; Devaux, D.; Chen, X. C.; Stone, G. M.; Balsara, N. P. Morphology-Conductivity Relationship of Single-Ion-Conducting Block Copolymer Electrolytes for Lithium Batteries. *ACS Macro Lett.* **2014**, *3*, 510–514.
- (14) Sanoja, G. E.; Popere, B. C.; Beckingham, B. S.; Evans, C. M.; Lynd, N. A.; Segalman, R. A. Structure-Conductivity Relationships of Block Copolymer Membranes Based on Hydrated Protic Polymerized Ionic Liquids: Effect of Domain Spacing. *Macromolecules* **2016**, 49, 2216–2223.
- (15) Elabd, Y. A. Ion transport in hydroxide conducting block copolymers. *Mol. Syst. Des. Eng.* **2019**, *4*, 519–530.
- (16) Galluzzo, M. D.; Loo, W. S.; Schaible, E.; Zhu, C.; Balsara, N. P. Dynamic Structure and Phase Behavior of a Block Copolymer Electrolyte under dc Polarization. *ACS Appl. Mater. Interfaces* **2020**, *12*, 57421–57430.
- (17) Meek, K. M.; Elabd, Y. A. Polymerized ionic liquid block copolymers for electrochemical energy. *J. Mater. Chem. A* **2015**, 3, 24187–24194.
- (18) Delhorbe, V.; Bresser, D.; Mendil-Jakani, H.; Rannou, P.; Bernard, L.; Gutel, T.; Lyonnard, S.; Picard, L. Unveiling the Ion Conduction Mechanism in Imidazolium-Based Poly(ionic liquids): A Comprehensive Investigation of the Structure-to-Transport Interplay. *Macromolecules* **2017**, *50*, 4309–4321.
- (19) Harris, M. A.; Heres, M. F.; Coote, J.; Wenda, A.; Strehmel, V.; Stein, G. E.; Sangoro, J. Ion Transport and Interfacial Dynamics in Disordered Block Copolymers of Ammonium-Based Polymerized Ionic Liquids. *Macromolecules* **2018**, *51*, 3477–3486.
- (20) Hashimoto, K.; Hirasawa, M.; Kokubo, H.; Tamate, R.; Li, X.; Shibayama, M.; Watanabe, M. Transport and Mechanical Properties of ABA-type Triblock Copolymer Ion Gels Correlated with Their Microstructures. *Macromolecules* **2019**, *52*, 8430–8439.
- (21) Sethuraman, V.; Mogurampelly, S.; Ganesan, V. Multiscale Simulations of Lamellar PS-PEO Block Copolymers Doped with LiPF6 Ions. *Macromolecules* **2017**, *50*, 4542–4554.
- (22) Seo, Y.; Brown, J. R.; Hall, L. M. Diffusion of Selective Penetrants in Interfacially Modified Block Copolymers from Molecular Dynamics Simulations. *ACS Macro Lett.* **2017**, *6*, 375–380.
- (23) Seo, Y.; Shen, K.-H.; Brown, J. R.; Hall, L. M. Role of Solvation on Diffusion of Ions in Diblock Copolymers: Understanding the Molecular Weight Effect through Modeling. *J. Am. Chem. Soc.* **2019**, 141, 18455–18466.

- (24) Alshammasi, M. S.; Escobedo, F. A. Correlation between Ionic Mobility and Microstructure in Block Copolymers. A Coarse-Grained Modeling Study. *Macromolecules* **2018**, *51*, 9213–9221.
- (25) Alshammasi, M. S.; Escobedo, F. A. Correlation between morphology and anisotropic transport properties of diblock copolymers melts. *Soft Matter* **2019**, *15*, 851–859.
- (26) Sharon, D.; Bennington, P.; Dolejsi, M.; Webb, M. A.; Dong, B. X.; de Pablo, J. J.; Nealey, P. F.; Patel, S. N. Intrinsic Ion Transport Properties of Block Copolymer Electrolytes. *ACS Nano* **2020**, *14*, 8902–8914.
- (27) Miranda, D. F.; Versek, C.; Tuominen, M. T.; Russell, T. P.; Watkins, J. J. Cross-Linked Block Copolymer/Ionic Liquid Self-Assembled Blends for Polymer Gel Electrolytes with High Ionic Conductivity and Mechanical Strength. *Macromolecules* **2013**, 46, 9313–9323.
- (28) Jung, H. Y.; Kim, S. Y.; Kim, O.; Park, M. J. Effect of the Protogenic Group on the Phase Behavior and Ion Transport Properties of Acid-Bearing Block Copolymers. *Macromolecules* **2015**, 48, 6142–6152.
- (29) Wang, R.-Y.; Guo, X.-S.; Fan, B.; Zou, S.-F.; Cao, X.-H.; Tong, Z.-Z.; Xu, J.-T.; Du, B.-Y.; Fan, Z.-Q. Design and Regulation of Lower Disorder-to-Order Transition Behavior in the Strongly Interacting Block Copolymers. *Macromolecules* **2018**, *51*, 2302–2311.
- (30) Forsyth, M.; Porcarelli, L.; Wang, X.; Goujon, N.; Mecerreyes, D. Innovative Electrolytes Based on Ionic Liquids and Polymers for Next-Generation Solid-State Batteries. *Acc. Chem. Res.* **2019**, 52, 686–694.
- (31) Mapesa, E. U.; Chen, M.; Heres, M. F.; Harris, M. A.; Kinsey, T.; Wang, Y.; Long, T. E.; Lokitz, B. S.; Sangoro, J. R. Charge Transport in Imidazolium-Based Homo- and Triblock Poly(ionic liquid)s. *Macromolecules* **2019**, 52, 620–628.
- (32) Russell, S. T.; Raghunathan, R.; Jimenez, A. M.; Zhang, K.; Brucks, S. D.; Iacob, C.; West, A. C.; Gang, O.; Campos, L. M.; Kumar, S. K. Impact of Electrostatic Interactions on the Self-Assembly of Charge-Neutral Block Copolyelectrolytes. *Macromolecules* **2020**, *53*, 548–557.
- (33) Coote, J. P.; Kinsey, T.; Street, D. P.; Kilbey, S. M.; Sangoro, J. R.; Stein, G. E. Surface-Induced Ordering Depresses Through-Film Ionic Conductivity in Lamellar Block Copolymer Electrolytes. *ACS Macro Lett.* **2020**, *9*, 565–570.
- (34) Choi, J.-H.; Ye, Y.; Elabd, Y. A.; Winey, K. I. Network Structure and Strong Microphase Separation for High Ion Conductivity in Polymerized Ionic Liquid Block Copolymers. *Macromolecules* **2013**, *46*, 5290–5300.
- (35) Choi, J.-H.; Xie, W.; Gu, Y.; Frisbie, C. D.; Lodge, T. P. Single Ion Conducting, Polymerized Ionic Liquid Triblock Copolymer Films: High Capacitance Electrolyte Gates for n-type Transistors. ACS Appl. Mater. Interfaces 2015, 7, 7294–7302.
- (36) Cordella, D.; Kermagoret, A.; Debuigne, A.; Jérôme, C.; Mecerreyes, D.; Isik, M.; Taton, D.; Detrembleur, C. All Poly(ionic liquid)-Based Block Copolymers by Sequential Controlled Radical Copolymerization of Vinylimidazolium Monomers. *Macromolecules* **2015**, *48*, 5230–5243.
- (37) Borodin, O.; Smith, G. D.; Henderson, W. Li+ Cation Environment, Transport, and Mechanical Properties of the LiTFSI Doped N-Methyl-N-alkylpyrrolidinium+TFSI-Ionic Liquids. *J. Phys. Chem. B* **2006**, *110*, 16879–16886.
- (38) Borodin, O.; Smith, G. D.; Geiculescu, O.; Creager, S. E.; Hallac, B.; DesMarteau, D. Li+ Transport in Lithium Sulfonylimide-Oligo(ethylene oxide) Ionic Liquids and Oligo(ethylene oxide) Doped with LiTFSI. *J. Phys. Chem. B* **2006**, *110*, 24266–24274.
- (39) Maitra, A.; Heuer, A. Cation Transport in Polymer Electrolytes: A Microscopic Approach. *Phys. Rev. Lett.* **2007**, *98*, 227802.
- (40) Diddens, D.; Heuer, A.; Borodin, O. Understanding the Lithium Transport within a Rouse-Based Model for a PEO/LiTFSI Polymer Electrolyte. *Macromolecules* **2010**, *43*, 2028–2036.
- (41) Sethuraman, V.; Mogurampelly, S.; Ganesan, V. Ion transport mechanisms in lamellar phases of salt-doped PS-PEO block copolymer electrolytes. *Soft Matter* **2017**, *13*, 7793–7803.

- (42) Mogurampelly, S.; Keith, J. R.; Ganesan, V. Mechanisms Underlying Ion Transport in Polymerized Ionic Liquids. *J. Am. Chem. Soc.* **2017**, *139*, 9511–9514.
- (43) Keith, J. R.; Mogurampelly, S.; Aldukhi, F.; Wheatle, B. K.; Ganesan, V. Influence of molecular weight on ion-transport properties of polymeric ionic liquids. *Phys. Chem. Chem. Phys.* **2017**, *19*, 29134—29145.
- (44) Keith, J. R.; Mogurampelly, S.; Wheatle, B. K.; Ganesan, V. Influence of side chain linker length on ion-transport properties of polymeric ionic liquids. *J. Polym. Sci., Part B: Polym. Phys.* **2017**, *SS*, 1718–1723.
- (45) Mogurampelly, S.; Ganesan, V. Ion Transport in Polymerized Ionic Liquid-Ionic Liquid Blends. *Macromolecules* **2018**, *51*, 9471–9483.
- (46) Zhang, Z.; Krajniak, J.; Keith, J. R.; Ganesan, V. Mechanisms of Ion Transport in Block Copolymeric Polymerized Ionic Liquids. *ACS Macro Lett.* **2019**, *8*, 1096–1101.
- (47) Keith, J. R.; Rebello, N. J.; Cowen, B. J.; Ganesan, V. Influence of Counterion Structure on Conductivity of Polymerized Ionic Liquids. *ACS Macro Lett.* **2019**, *8*, 387–392.
- (48) Keith, J. R.; Ganesan, V. Ion transport in backbone-embedded polymerized ionic liquids. *J. Chem. Phys.* **2019**, *151*, 124902.
- (49) Keith, J. R.; Ganesan, V. Ion transport mechanisms in salt-doped polymerized zwitterionic electrolytes. *J. Polym. Sci.* **2020**, *58*, 578–588.
- (50) Shen, K.-H.; Brown, J. R.; Hall, L. M. Diffusion in Lamellae, Cylinders, and Double Gyroid Block Copolymer Nanostructures. *ACS Macro Lett.* **2018**, *7*, 1092–1098.
- (51) Shen, K.-H.; Hall, L. M. Ion Conductivity and Correlations in Model Salt-Doped Polymers: Effects of Interaction Strength and Concentration. *Macromolecules* **2020**, *53*, 3655–3668.
- (52) Aryal, D.; Howard, M. P.; Samanta, R.; Antoine, S.; Segalman, R.; Truskett, T. M.; Ganesan, V. Influence of pore morphology on the diffusion of water in triblock copolymer membranes. *J. Chem. Phys.* **2020**, *152*, 014904.
- (53) Nakamura, I.; Balsara, N. P.; Wang, Z.-G. Thermodynamics of Ion-Containing Polymer Blends and Block Copolymers. *Phys. Rev. Lett.* **2011**, *107*, 198301.
- (54) Ganesan, V.; Pyramitsyn, V.; Bertoni, C.; Shah, M. Mechanisms Underlying Ion Transport in Lamellar Block Copolymer Membranes. *ACS Macro Lett.* **2012**, *1*, 513–518.
- (55) Seo, Y.; Brown, J. R.; Hall, L. M. Effect of Tapering on Morphology and Interfacial Behavior of Diblock Copolymers from Molecular Dynamics Simulations. *Macromolecules* **2015**, *48*, 4974–4982
- (56) Ryu, J. H.; Wee, H. S.; Lee, W. B. Molecular dynamics study on microstructures of diblock copolymer melts with soft potential and potential recovery. *Phys. Rev. E: Stat. Phys., Plasmas, Fluids, Relat. Interdiscip. Top.* **2016**, *94*, 32501.
- (57) Kumar, R.; Li, W.; Sumpter, B. G.; Muthukumar, M. Understanding the effects of dipolar interactions on the thermodynamics of diblock copolymer melts. *J. Chem. Phys.* **2019**, *151*, 054902.
- (58) Daoulas, K. C.; Müller, M. Single chain in mean field simulations: Quasi-instantaneous field approximation and quantitative comparison with Monte Carlo simulations. *J. Chem. Phys.* **2006**, *125*, 184904
- (59) Daoulas, K. C.; Müller, M.; de Pablo, J. J.; Nealey, P. F.; Smith, G. D. Morphology of multi-component polymer systems: single chain in mean field simulation studies. *Soft Matter* **2006**, *2*, 573–583.
- (60) Daoulas, K. C.; Rühle, V.; Kremer, K. Simulations of nematic homopolymer melts using particle-based models with interactions expressed through collective variables. *J. Phys.: Condens. Matter* **2012**, 24, 284121.
- (61) Detcheverry, F. b. çA.; Pike, D. Q.; Nealey, P. F.; Müller, M.; de Pablo, J. J. Monte Carlo Simulation of Coarse Grain Polymeric Systems. *Phys. Rev. Lett.* **2009**, *102*, 197801.
- (62) Müller, M.; de Pablo, J. J. Computational Approaches for the Dynamics of Structure Formation in Self-Assembling Polymeric Materials. *Annu. Rev. Mater. Res.* **2013**, *43*, 1–34.

- (63) Peter, C.; Kremer, K. Multiscale simulation of soft matter systems from the atomistic to the coarse-grained level and back. *Soft Matter* **2009**, *5*, 4357–4366.
- (64) Davtyan, A.; Dama, J. F.; Voth, G. A.; Andersen, H. C. Dynamic force matching: A method for constructing dynamical coarse-grained models with realistic time dependence. *J. Chem. Phys.* **2015**, *142*, 154104.
- (65) Davtyan, A.; Voth, G. A.; Andersen, H. C. Dynamic force matching: Construction of dynamic coarse-grained models with realistic short time dynamics and accurate long time dynamics. *J. Chem. Phys.* **2016**, *145*, 224107.
- (66) Xiao, Q.; Guo, H. Transferability of a coarse-grained atactic polystyrene model: the non-bonded potential effect. *Phys. Chem. Chem. Phys.* **2016**, *18*, 29808–29824.
- (67) Xia, J.; Xiao, Q.; Guo, H. Transferability of a coarse-grained atactic polystyrene model: Thermodynamics and structure. *Polymer* **2018**, *148*, 284–294.
- (68) Reith, D.; Pütz, M.; Müller-Plathe, F. Deriving effective mesoscale potentials from atomistic simulations. *J. Comput. Chem.* **2003**, *24*, 1624–1636.
- (69) Moore, T. C.; Iacovella, C. R.; McCabe, C. Derivation of coarse-grained potentials via multistate iterative Boltzmann inversion. *J. Chem. Phys.* **2014**, *140*, 224104.
- (70) Agrawal, V.; Arya, G.; Oswald, J. Simultaneous Iterative Boltzmann Inversion for Coarse-Graining of Polyurea. *Macromolecules* **2014**, *47*, 3378–3389.
- (71) Rosenberger, D.; Hanke, M.; van der Vegt, N. F. A. Comparison of iterative inverse coarse-graining methods. *Eur. Phys. J.: Spec. Top.* **2016**, 225, 1323–1345.
- (72) Pronk, S.; Páll, S.; Schulz, R.; Larsson, P.; Bjelkmar, P.; Apostolov, R.; Shirts, M. R.; Smith, J. C.; Kasson, P. M.; van der Spoel, D.; Hess, B.; Lindahl, E. GROMACS 4.5: a high-throughput and highly parallel open source molecular simulation toolkit. *Bioinformatics* 2013, 29, 845–854.
- (73) Becke, A. D. Density-functional thermochemistry. III. The role of exact exchange. *J. Chem. Phys.* **1993**, *98*, 5648–5652.
- (74) Lee, C.; Yang, W.; Parr, R. G. Development of the Colle-Salvetti correlation-energy formula into a functional of the electron density. *Phys. Rev. B: Condens. Matter Mater. Phys.* **1988**, 37, 785–789.
- (75) Krishnan, R.; Binkley, J. S.; Seeger, R.; Pople, J. A. Self-consistent molecular orbital methods. XX. A basis set for correlated wave functions. *J. Chem. Phys.* **1980**, 72, 650–654.
- (76) Frisch, M. J.; et al. Gaussian 09, rev. E.01; Gaussian Inc.: Wallingford, CT, 2009.
- (77) Lu, T.; Chen, F. Multiwfn: A multifunctional wavefunction analyzer. J. Comput. Chem. 2012, 33, 580-592.
- (78) Ribeiro, A. A. S. T.; Horta, B. A. C.; de Alencastro, R. B. MKTOP: a program for automatic construction of molecular topologies. *J. Braz. Chem. Soc.* **2008**, *19*, 1433–1435.
- (79) Martínez, L.; Andrade, R.; Birgin, E. G.; Martínez, J. M. PACKMOL: A package for building initial configurations for molecular dynamics simulations. *J. Comput. Chem.* **2009**, *30*, 2157–2164.
- (80) Darden, T.; York, D.; Pedersen, L. Particle mesh Ewald: An N-log(N) method for Ewald sums in large systems. *J. Chem. Phys.* **1993**, 98, 10089–10092.
- (81) Evans, D. J.; Holian, B. L. The Nosé-Hoover thermostat. *J. Chem. Phys.* **1985**, 83, 4069-4074.
- (82) Parrinello, M.; Rahman, A. Polymorphic transitions in single crystals: A new molecular dynamics method. *J. Appl. Phys.* **1981**, *52*, 7182–7190.
- (83) Hess, B.; Bekker, H.; Berendsen, H. J. C.; Fraaije, J. G. E. M. LINCS: A linear constraint solver for molecular simulations. *J. Comput. Chem.* **1997**, *18*, 1463–1472.
- (84) Larsen, G. S.; Lin, P.; Hart, K. E.; Colina, C. M. Molecular Simulations of PIM-1-like Polymers of Intrinsic Microporosity. *Macromolecules* **2011**, *44*, 6944–6951.
- (85) Hart, K. E.; Abbott, L. J.; McKeown, N. B.; Colina, C. M. Toward Effective CO₂/CH4 Separations by Sulfur-Containing PIMs

- via Predictive Molecular Simulations. *Macromolecules* **2013**, 46, 5371–5380.
- (86) Rühle, V.; Junghans, C.; Lukyanov, A.; Kremer, K.; Andrienko, D. Versatile Object-Oriented Toolkit for Coarse-Graining Applications. *J. Chem. Theory Comput.* **2009**, *5*, 3211–3223.
- (87) Zhang, Z.; Wang, L.; Wang, Z.; He, X.; Chen, Y.; Mueller-Plathe, F.; Boehm, M. C. A coarse-grained molecular dynamics reactive Monte Carlo approach to simulate hyperbranched polycondensation. *RSC Adv.* **2014**, *4*, 56625–56636.
- (88) Zhang, Z.; Krajniak, J.; Samaey, G.; Nies, E. A Parallel Multiscale Simulation Framework for Complex Polymerization: AB2-Type Monomer Hyperbranched Polymerization as an Example. Advanced Theory and Simulations 2019, 2, 1800102.
- (89) Weeks, J. D.; Chandler, D.; Andersen, H. C. Role of Repulsive Forces in Determining the Equilibrium Structure of Simple Liquids. *J. Chem. Phys.* **1971**, *54*, 5237–5247.
- (90) Krajniak, J.; Pandiyan, S.; Nies, E.; Samaey, G. Generic Adaptive Resolution Method for Reverse Mapping of Polymers from Coarse-Grained to Atomistic Descriptions. *J. Chem. Theory Comput.* **2016**, *12*, 5549–5562.
- (91) Krajniak, J.; Zhang, Z.; Pandiyan, S.; Nies, E.; Samaey, G. Reverse mapping method for complex polymer systems. *J. Comput. Chem.* **2018**, 39, 648–664.
- (92) Praprotnik, M.; Delle Site, L.; Kremer, K. Adaptive resolution molecular-dynamics simulation: changing the degrees of freedom on the fly. *J. Chem. Phys.* **2005**, *123*, 224106–224120.
- (93) Krajniak, J.; Zhang, Z. Bakery: reverse mapping tool master branch. 2019; https://github.com/bakery-cg2at/bakery/tree/master.
- (94) Goga, N.; Rzepiela, A. J.; de Vries, A. H.; Marrink, S. J.; Berendsen, H. J. C. Efficient Algorithms for Langevin and DPD Dynamics. *J. Chem. Theory Comput.* **2012**, *8*, 3637–3649.
- (95) Krajniak, J. Molecular dynamics code for reverse mapping based on the adaptive resolution scheme method. 2019; https://github.com/bakery-cg2at/espressopp.
- (96) Guzman, H. V.; Tretyakov, N.; Kobayashi, H.; Fogarty, A. C.; Kreis, K.; Krajniak, J.; Junghans, C.; Kremer, K.; Stuehn, T. ESPResSo ++ 2.0: Advanced methods for multiscale molecular simulation. *Comput. Phys. Commun.* **2019**, 238, 66–76.
- (97) Zhang, Z.; Wheatle, B. K.; Krajniak, J.; Keith, J. R.; Ganesan, V. Ion Mobilities, Transference Numbers, and Inverse Haven Ratios of Polymeric Ionic Liquids. ACS Macro Lett. 2020, 9, 84–89.